AGU100 ADVANCING EARTH AND SPACE SCIENCE

Journal of Advances in Modeling Earth Systems

RESEARCH ARTICLE
10.1029/2018MS001416

Organization and Oscillations in Simulated Shallow Convective Clouds

Guy Dagan[1], Ilan Koren[1], Alex Kostinski[2], and Orit Altaratz[1]

[1]Department of Earth and Planetary Sciences, The Weizmann Institute of Science, Rehovot, Israel, [2]Physics Department, Michigan Technological University, Houghton, MI, USA

Key Points:
- Large eddy simulations with bin microphysics used to study spatial and temporal organization in shallow convective cloud fields
- Warm convective cloud fields exhibit oscillations with two distinct periods
- Low frequency is driven by recharge-discharge cycles of thermodynamic instability, high frequency by gravity waves

Supporting Information:
- Supporting Information S1

Correspondence to:
I. Koren,
ilan.koren@weizmann.ac.il

Citation:
Dagan, G., Koren, I., Kostinski, A., & Altaratz, O. (2018). Organization and oscillations in simulated shallow convective clouds. *Journal of Advances in Modeling Earth Systems, 10*, 2287–2299. https://doi.org/10.1029/2018MS001416

Received 19 JUN 2018
Accepted 6 AUG 2018
Accepted article online 3 SEP 2018
Published online 22 SEP 2018

Abstract Physical insights into processes governing temporal organization and evolution of cloud fields are of great importance for climate research. Here using large eddy simulations with a bin microphysics scheme, we show that warm convective cloud fields exhibit oscillations with two distinct periods (~10 and ~90 min, for the case studied here). The shorter period dominates the nonprecipitating phase, and the longer period is related to the precipitating phase. We show that rain processes affect the domain's thermodynamics, hence forcing the field into a low-frequency *recharge-discharge* cycle of developing cloudiness followed by precipitation-driven depletion. The end result of precipitation is stabilization of the lower atmosphere by warming of the cloudy layer (due to latent heat release) and cooling of the subcloud layer (by rain evaporation, creating cold pools). As the thermodynamic instability weakens, so does the cloudiness, and the rain ceases. During the nonprecipitating phase of the cycle, surface fluxes destabilize the boundary layer until the next precipitation cycle. Under conditions that do not allow development of precipitation (e.g., high aerosol loading), high-frequency oscillations dominate the cloud field. Clouds penetrating the stable inversion layer trigger gravity waves with a typical period of ~10 min. In return, the gravity waves modulate the clouds in the field by modifying the vertical velocity, temperature, and humidity fields. Subsequently, as the polluted nonprecipitating simulations evolve, the thermodynamic instability increases and the cloudy layer deepens until precipitation forms, shifting the oscillations from high to low frequency. The organization of cold pools and the spatial scale related to these oscillations are explored.

Plain Language Summary Large eddy simulations with bin microphysics are used to study spatial and temporal organization in shallow convective cloud fields. It is shown that warm convective cloud fields exhibit oscillations with two distinct periods of ~10 and ~90 min. The low frequency is driven by *recharge-discharge* cycles of thermodynamic instability, while the high frequency is driven by gravity waves.

1. Introduction

Warm convective clouds are ubiquitous over the oceans (Norris, 1998) and play an important role in the boundary layer's energy and moisture budgets. Moreover, these clouds are responsible for the largest uncertainty in tropical cloud feedback in climate models (Bony & Dufresne, 2005; Webb et al., 2006), and their properties often cannot be obtained from space-based observations due to resolution limitations (Platnick et al., 2003). Hence, understanding the processes controlling their properties is of great importance.

Both the internal dynamics of warm cloud fields (referred to as self-organization) and external forcing factors (such as sharp changes in the surface properties) tend to organize the clouds into detectable patterns. Trade cumulus clouds exhibit a range of organization levels from fields that appear to be almost randomly distributed to strict patterns such as cloud streets, clusters, or mesoscale arcs (Malkus & Riehl, 1964; Nair et al., 1998; Seifert & Heus, 2013). Such organization was recently suggested to play a role in low-cloud feedback to global warming (Vogel et al., 2016) because of its effect on clouds' properties and on the clouds' effect on the thermodynamic condition.

Organization can be determined as a deviation from randomness in the spatial and temporal domains. It can manifest as emerging spatial patterns (see examples in Figure 1) and as temporal oscillations in key cloud properties (such as total mass, total rain, and cloud cover). Several self-organization mechanisms have been previously proposed for shallow cloud fields related to gravity waves and precipitation.

Gravity waves (a wave disturbance in which buoyancy acts as a restoring force on parcels displaced from hydrostatic equilibrium, Nappo, 2013) can be generated by clouds that penetrate a stable atmospheric

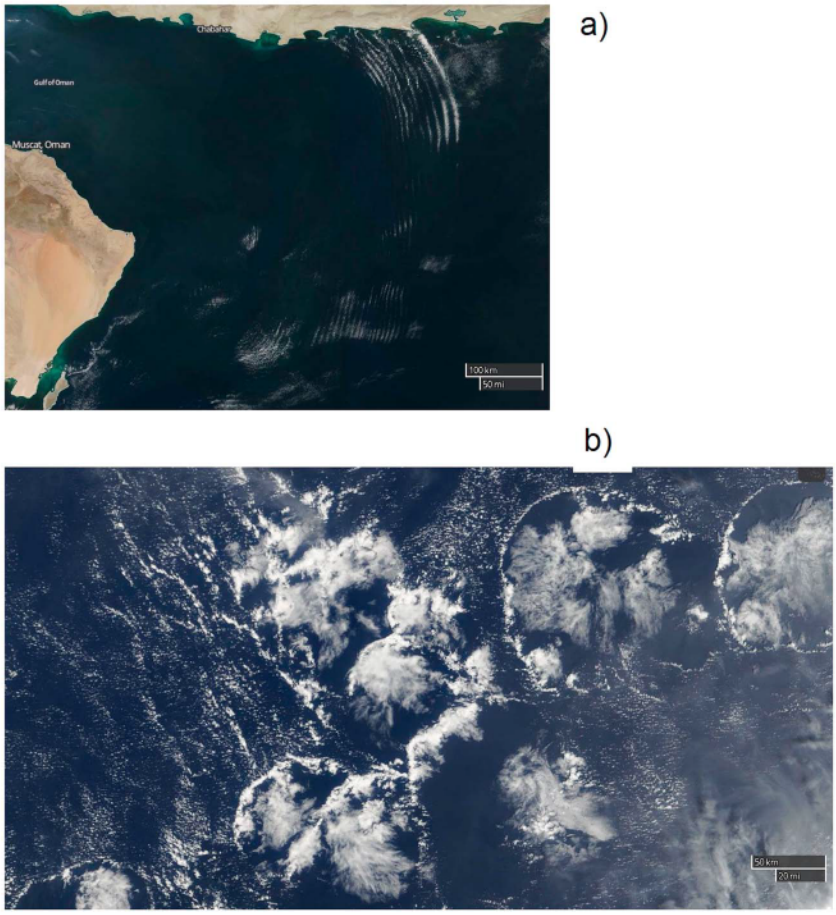

Figure 1. Examples of organized warm cloud fields. (a) Gravity waves that generate warm clouds. This satellite image was taken by MODIS (Moderate Resolution Imaging Spectroradiometer) Terra (Platnick et al., 2003) on 12 November 2004, and it covers the Arabian Sea (20.2°–25.4°N and 58.1°–65.2°W). (b) Mesoscale cloud arcs. This satellite image was taken by MODIS Terra on 11 March 2002, and it covers the Pacific Ocean near Marshall Islands (10.1°–12.5°N, 198.5°–203.3°W).

layer and produce perturbations in it. This process modulates the formation of the next generation of clouds by changing the updraft, temperature, and humidity fields in parts of the atmospheric profile, which generate additional gravity waves, and so on (Huang, 1990). Areas with negative air vertical velocity (due to the gravity waves) slightly inhibit cloud development, while areas with positive vertical velocity encourage it. Hence, it has been proposed as a cloud self-organization mechanism (Atkinson & Zhang, 1996; Clark et al., 1986; Huang, 1990).

Changes in rain properties are a key factor in facilitating high levels of organization of warm convective cloud fields (Heiblum et al., 2016; Seifert & Heus, 2013; Seigel, 2014; Xue et al., 2008). The link between rain and organization relates to rain evaporation below the cloud base that generates cold pools (Zuidema et al., 2012) near the surface (Heiblum et al., 2016; Seifert & Heus, 2013). The negatively buoyant cold pools affect the spatial organization of the clouds by reducing the likelihood of convective thermals originating beneath the clouds from reaching cloud base level and promoting cloud generation at their boundaries (Heiblum et al., 2016; Seifert & Heus, 2013; Seigel, 2014).

Temporal oscillations have been reported for marine stratocumulus precipitating clouds (Feingold et al., 2010; Koren et al., 2017; Koren & Feingold, 2011). Evaporative cooling of rain below the cloud base promotes downdrafts that reach the surface, diverge, and collide with the outflows of neighboring precipitating cells. The convergence due to the collision of outflows near the surface generates updrafts and new cloud formation (Feingold & Koren, 2013; Koren & Feingold, 2013), thus generating both spatial organization and temporal oscillations.

Temporal oscillations have been also reported for deep convective clouds (i.e. Yano & Plant, 2012). In this case, cycles of recharge-discharge of thermodynamic instability were identified (Bladé & Hartmann, 1993). Those cycles were explained as follow: once sufficient convective potential energy accumulates in the atmosphere the convection begins, hereafter it reduces (consumes) the instability, until the convection stops. Next the instability builds up again until launching another cycle (Yano & Plant, 2012). These oscillations were suggested to play a key role in Madden-Julian oscillation (Benedict & Randall, 2007; Thayer-Calder & Randall, 2009).

Aerosols acting as cloud condensation nuclei have been shown to influence warm convective clouds' processes, including rain formation, and hence to affect all of the abovementioned organization mechanisms (Dagan et al., 2015a, 2015b; Dey et al., 2011; Jiang et al., 2006; Koren et al., 2014; Rosenfeld, 1999; Rosenfeld et al., 2013; Savane et al., 2015; Small et al., 2009; Xue & Feingold, 2006; Yuan et al., 2011). Elevated aerosol loading has been shown to fully suppress rain formation in marine stratocumulus clouds, conferring a closed cell structure (Goren & Rosenfeld, 2012; Rosenfeld et al., 2006) for which no oscillations are observed (Feingold & Koren, 2013; Koren & Feingold, 2011). In addition, aerosol concentration has been shown to affect the clouds' impact on their environment (Dagan et al., 2016), that is, shallow convective clouds developing in a polluted environment act to increase thermodynamic instability with time, whereas clean clouds consume it.

Here we explore the self-organization mechanisms of warm marine cumulus clouds under a wide range of aerosol conditions, using large eddy simulations (LES) with bin microphysics. Understanding such mechanisms of organization is likely to yield a better understanding of both cloud-aerosol interactions, which have been shown to be mediated by cloud organization (Seifert et al., 2015), and low-cloud feedback, which has been shown to be sensitive to cloud organization due to the latter's effect on the cloud properties (Vogel et al., 2016).

2. Methodology

The BOMEX (Barbados Oceanographic and Meteorological Experiment) case study of trade cumulus clouds (Holland & Rasmusson, 1973; Siebesma et al., 2003) is simulated by the System for Atmospheric Modeling, nonhydrostatic, anelastic LES model, version 6.10.3 (Khairoutdinov & Randall, 2003). The BOMEX case study is based on observations made near Barbados in June 1969. The simulations are initialized using the setup specified in Siebesma et al. (2003), which includes large-scale forcing (see details in Dagan et al., 2016) and surface fluxes that are prescribed in all simulations. The horizontal resolution is set to 100 m and the vertical resolution to 40 m. We use two different domain sizes in the simulations: a small domain of $12.8 \times 12.8 \times 4.0\ km^3$ and a large domain of $51.2 \times 51.2 \times 4.0\ km^3$ (unless otherwise noted, the small domain results are presented). The time step is 1 s, and the simulation periods are 8, 16, or 32 hr depending on the specific simulation. The first 2 hr of all simulations are excluded from the statistical analysis (considered as spin-up time).

We use a bin microphysics scheme that solves warm microphysical processes, including droplet nucleation, diffusional growth, collision coalescence, sedimentation, and breakup (Khain & Pokrovsky, 2004). Six different aerosol-loading conditions are simulated, from extremely pristine to polluted (total concentrations of: 5, 50, 100, 500, 2,000, and $5{,}000/cm^3$ near ground level). We use a marine aerosol size distribution (see details in Jaenicke, 1988; Altaratz et al., 2008) and a scaler to determine the initial integrated concentration. This approach reduces the results' sensitivity to the shape of the aerosol size distribution and focuses on examining the effect of the aerosol number concentration. The aerosol amount is initialized with a constant mixing ratio with height, and it is assumed to be composed of ammonium sulfate. Activation of the aerosols is based on the Kohler theory (the scheme is described in Khain et al., 2000). A prognostic equation is solved for the aerosol mass, including removal by wet scavenging (surface rain) and regeneration upon drop evaporation. There is no external aerosol source; hence, under precipitating conditions the total aerosol concentration decreases with time (Heiblum et al., 2016). The aerosol and water drop size distributions are calculated from 5 nm to 2 μm and 2 μm to 3.2 mm, respectively. For both aerosol and drops, successive bins represent doubling of the mass.

It was recently shown that only below a grid size as small as 10 m a good numerical convergence is achieved for predicting the cloud cover in simulated shallow convection (Sato et al., 2017, 2018). Here due to limited

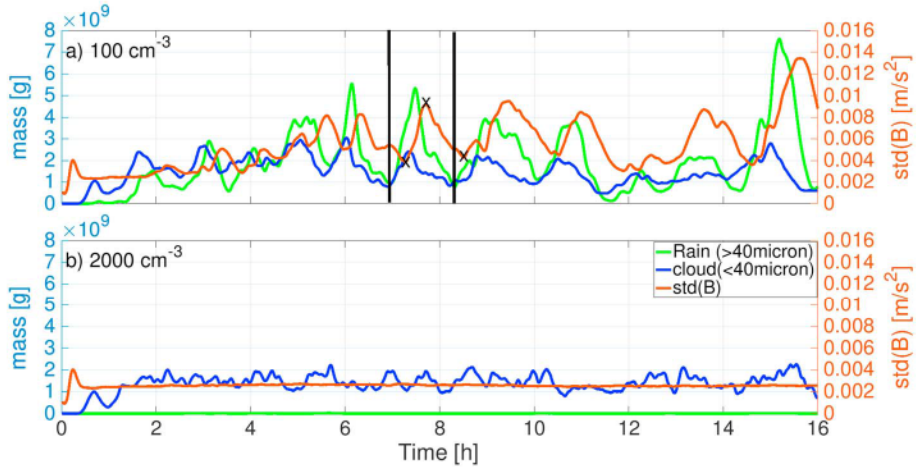

Figure 2. Temporal evolution of total cloud (blue) and rain (green) masses in the domain and standard deviation of the buoyancy near the surface (std (B)—brown) for simulations with aerosol concentrations of (a) 100 and (b) 2,000 cm^{-3}. The two different mass categories are defined according to a 40-μm threshold for drop radius. The black vertical lines and *x* mark one oscillation period (~90 min) which is further analyzed below.

computational resources (as we use bin microphysics, and relatively large domain for long simulations), we are unable to use such high resolution.

3. Results and Discussion

To set the stage, we explore the evolution of two representative simulations: clean (with aerosol concentration of 100 cm^{-3}) and polluted (2,000 cm^{-3}). Figure 2 presents the evolution of the total cloud mass (blue curve) and rain mass (green curve) in the domains of the two simulations. Under clean conditions (Figure 2a), the water mass (including both cloud and rain masses) oscillates in time, with a dominant frequency of ~90 min. On the other hand, under polluted conditions (Figure 2b), where there is no rain and all of the water mass is attributed to cloud droplets, it oscillates at high frequency with a typical time period of ~10 min.

Beside the evolution of the cloud and rain masses, Figure 2 presents the evolution of the standard deviation of the buoyancy (std(B)) near the surface (at altitude of 20 m, the lowest grid cell). We note that under clean precipitating conditions (Figure 2a), in which the cloud and rain masses oscillate with time, the std (B) oscillates as well, with a similar periodicity (~90 min) but with a shift in time (~20 min delay after the rain mass oscillations). On the other hand, under polluted nonprecipitating conditions (Figure 2b), std (B) is almost constant with time and it is lower than the clean case values (Figure 2a). The std (B) can be used as a measure of the magnitude of the cold pools in the domain. The rain that evaporates below the cloud base produces cold pools (Zuidema et al., 2012), and this increases the partition of the buoyancy field near the surface into designated areas of strong negative buoyancy (cold pools) surrounded by areas of strong positive buoyancy.

Under polluted nonprecipitating conditions, there are no cold pools (Figures 3d–3f). The impact of cold pools on cloud spatial organization is shown by the black contours. Note that the clouds tend to be larger and clustered (with larger cloud-free regions in the domain) under clean conditions, whereas under polluted conditions, clouds are smaller in size and distributed more uniformly over the domain. Such organization patterns and the link to cold pools have been shown previously (Heiblum et al., 2016; Seifert & Heus, 2013; Seigel, 2014; Xue et al., 2008). A similar oscillation periodicity of ~90 min has been shown for simulated warm cumulus cloud fields (see Figure 2 in Seigel, 2014) and from satellite obsrvations of open cells (Koren & Feingold, 2013).

To further examine the dominant frequency of the water mass oscillations in the different simulations (conducted under different aerosol-loading conditions), we calculated the total water mass cumulative power spectrum as a function of time for four simulations (Figure 4). This demonstrates that under clean

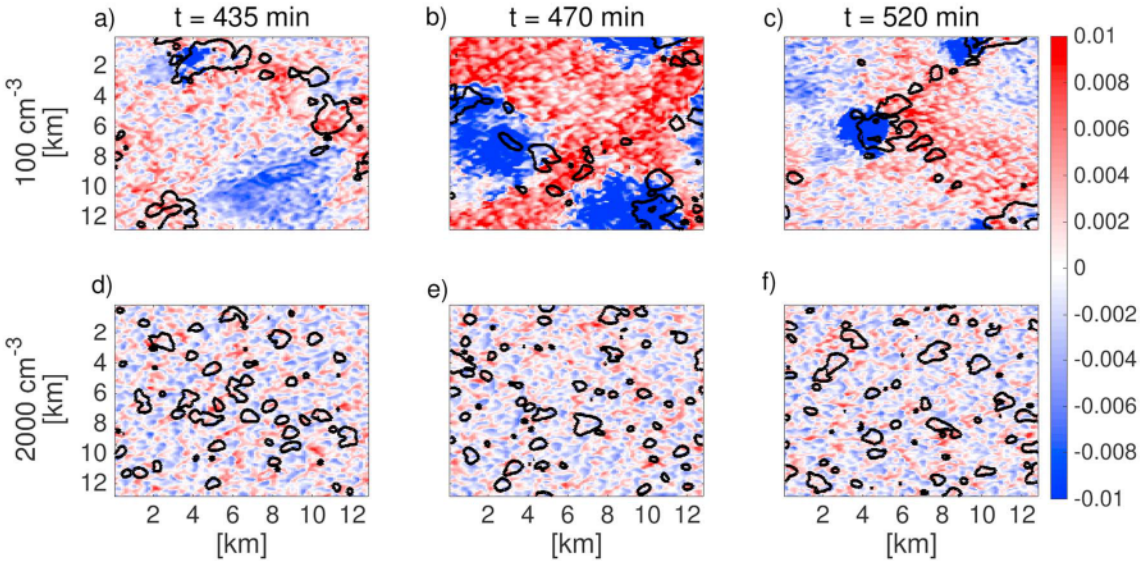

Figure 3. Buoyancy near the surface of the domain (at a height of 20 m, red-blue color bar [m/s^2]) and cloud cover (liquid water path >10 g/m^2, black contours). (a–c) Clean precipitating simulation with aerosol concentration of 100 cm^{-3}; (d–f) Polluted nonprecipitating simulation with aerosol concentration of 2,000 cm^{-3}. Each column presents different times of the simulations: 435 min (a and d), 470 min (b and e), and 520 min (c and f). These three times are marked by x in Figure 2a.

conditions (5 and 100 cm^{-3}), the cumulative power spectrum increases gradually during the short periods (<60 min) and it changes into a sharper slope at ~90 min (1.5 hr). On the other hand, under polluted conditions (500 and 5,000 cm^{-3}), the cumulative power spectrum increases more sharply in the short periods, suggesting higher contribution of high-frequency oscillations.

The results presented in Figures 2 and 4 demonstrate a shift between two dominant oscillation periods of ~10 min (dominant under polluted nonprecipitating conditions) and ~90 min (dominant under clean precipitating conditions). We focus next on the physical mechanisms that dictate the frequency of the oscillations.

Starting with the low-frequency cases, Figure 5 presents the evolution of one oscillation cycle on two phase spaces: cloud mass versus rain mass (Figure 5a) and total mass (rain + cloud mass) versus std (B) (Figure 5b). Figure S1 in the supporting information presents few oscillations on these two phase spaces for demonstrating the robustness of the cycles. This specific cycle is marked in Figure 2a by two vertical black lines (at 413 to 500 min of simulation). The oscillation cycle starts with an increase in the cloud mass (red arrow in Figure 5a)

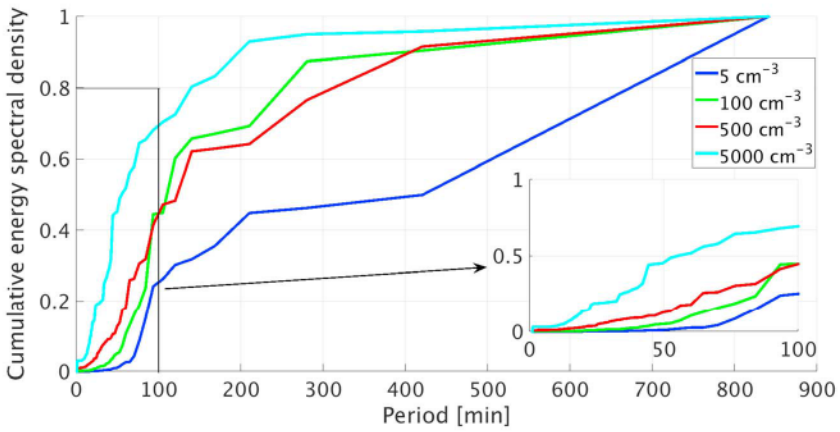

Figure 4. Cumulative power spectrum of the total water mass in the domain as a function of time for four different aerosol conditions (5, 100, 500, and 5,000 cm^{-3}).

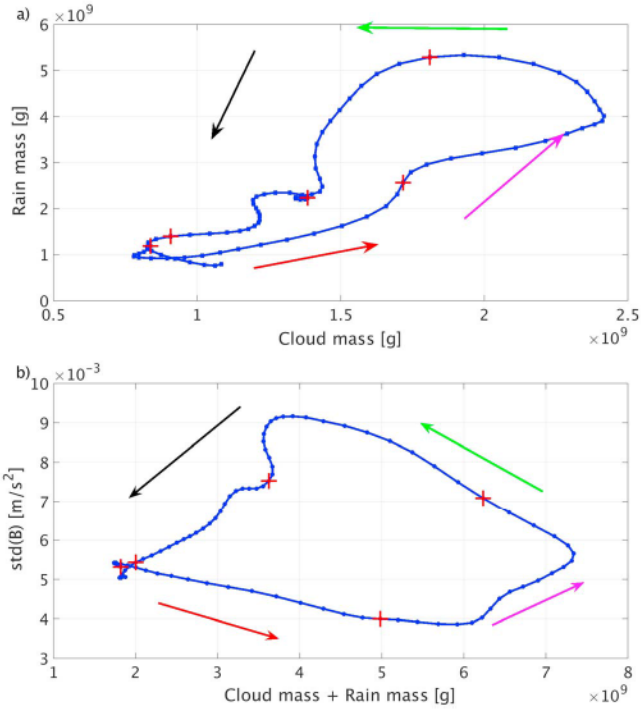

Figure 5. The evolution of a single oscillation on (a) cloud mass versus rain mass phase space and (b) total mass (cloud + rain mass) versus standard deviation of the buoyancy near the surface (std (B)) phase space. The oscillation presented here is the one marked by two black lines in Figure 2a. Blue dots and red crosses represent 1- and 20-min intervals, respectively.

followed by an increase in the rain mass (a delay of a few minutes, pink arrow in Figure 5a) and then a decrease in both of them in the same order (green and black arrows in Figure 5a, respectively). The cycle evolution on the total mass versus std (B) phase space (Figure 5b) demonstrates that std (B) (representing the cold pool magnitude) follows the total mass and oscillates with the same periodicity but with a time shift of ~20 min (see also Figure 2a).

To further explore the processes that dictate these oscillations, we followed the changes in the domain-mean thermodynamic conditions. Figure 6a presents the changes in the mean temperature vertical profile between successive time lags of 1 min, while Figure 6b presents the evolution of the temperature difference (lapse rate) between the inversion base height (1,500 m) and the lowest atmospheric grid cell (20 m). This represents the lower atmosphere convective instability—larger negative values represent greater instability.

Figure 6 presents an analysis of the relatively clean and therefore precipitating simulation. Under these conditions, the domain-mean convective instability decreases with time, meaning the lower atmosphere stabilizes (Dagan et al., 2016). The results shown in Figure 6 explain this trend by warming of the cloudy layer (~500–1,500 m) and cooling of the subcloud layer. A similar mechanism also acts at distinct shorter times that correspond to the typical time scale of the water mass oscillations (~90 min) as shown in Figure 2a. Each cycle can be described by a sequence of processes (as can be seen in Figure 6a) that starts with warming of the subcloud layer followed by strong warming of the cloudy layer, and later cooling of the subcloud layer (intensification of the cold pools' magnitude—Figure 2a). This sequence represents a recharge-discharge cycle of atmospheric instability. During the rain intermission, the surface fluxes warm and moisten the subcloud layer and hence recharge the instability. This destabilization drives vigorous cloud development that leads to warming of the cloudy layer by latent heat release (as can be seen in Figure 7). The condensed water sediments down as rain and partially evaporates below the cloud base (Figure 7), cooling the subcloud layer. Both the warming of the cloudy layer and the

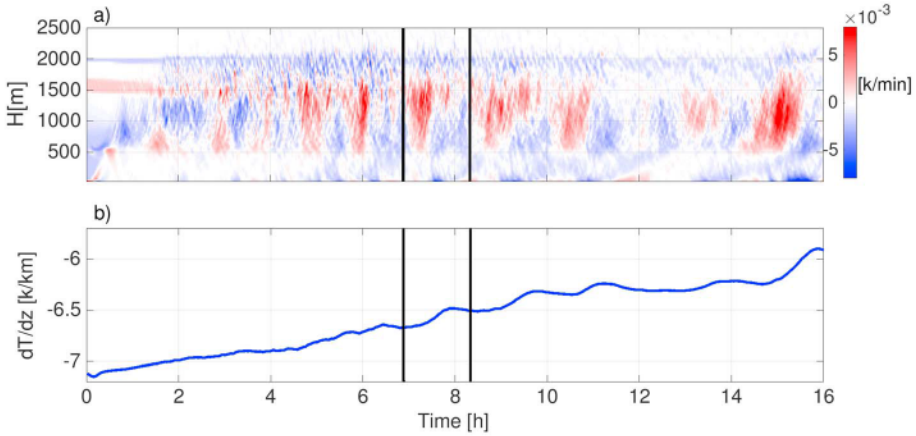

Figure 6. Temporal evolution of (a) the change between sequenced time steps (of 1 min) in mean temperature vertical profile in the domain (K/min) for the simulation with aerosol concentration of 100 cm^{-3}. (b) Temperature lapse rate (K/km) between the initial inversion base height (H = 1,500 m) and the lowest atmospheric grid cell (H = 20 m). The black vertical lines represent one oscillation cycle (~90 min) as in Figure 2a.

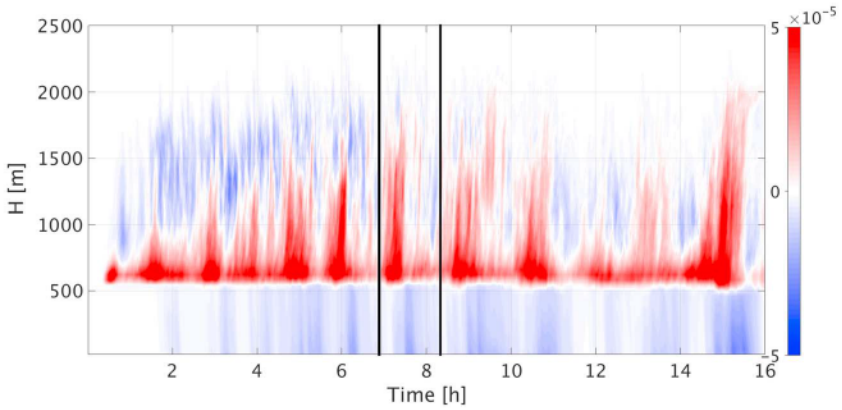

Figure 7. Temporal evolution of the domain-mean condensation-evaporation vertical profile (g/kg/s) for the simulation with aerosol concentration of 100 cm^{-3}. The black vertical lines represent one oscillation period (~90 min) as in Figure 2a.

cooling of the subcloud layer stabilize the lower atmosphere and hence reduce cloud and rain development. Once the rain stops, the surface fluxes start to rebuild the instability, and so forth.

How does the domain size affect the coherency of the oscillations? The results demonstrated above are the run outputs of a relatively small domain (12.8 × 12.8 km^2), and hence, periods of significant precipitation manage to stabilize the whole domain. However, we can speculate that in a larger domain, different regions will not be so well synchronized and therefore, local oscillations might be smoothed out by others that are in a different phase. This leads to the question of what spatial scale is relevant to these oscillations, or what is the right spatial scale to detect them? To answer this question, we conducted three additional simulations with a larger domain of 51.2 × 51.2 km^2 (similar to Seifert & Heus, 2013), using aerosol concentrations of 5, 50, and 500 cm^{-3} and no background winds (for easier tracking of cloud evolution). All larger domain simulations were conducted for 8 hr.

Figure 8 presents the evolution of the cloud and rain masses for different subdomains within the large domain (for the simulation with aerosol concentration of 50 cm^{-3}). For the entire domain (51.2 × 51.2 km^2; Figure 8a), the two curves (of the cloud and rain masses) are relatively smooth and no significant oscillations are observed. Decreasing the window size down to 12.8 × 12.8 km^2 (Figure 8c) or even 6.4 × 6.4 km^2

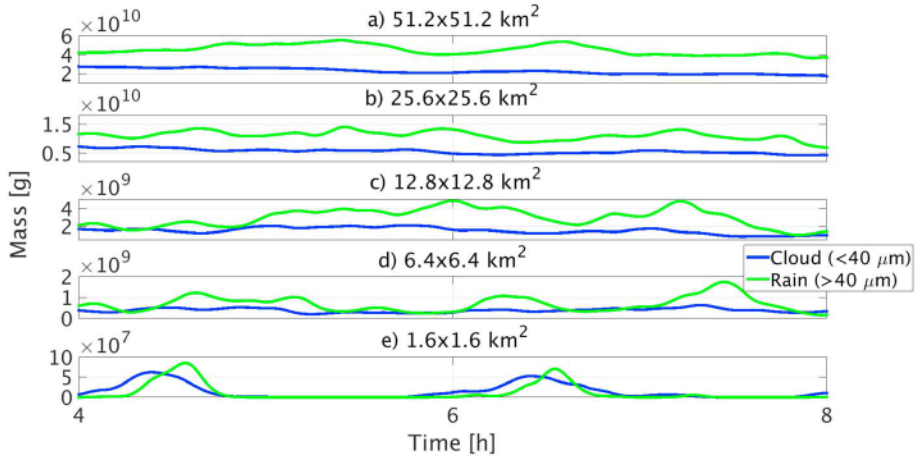

Figure 8. Evolution of the total cloud and rain masses in the domain for different subdomains in the simulation conducted with a large domain and aerosol concentration of 50 cm^{-3}. The different subdomains presented are (a) 51.2 × 51.2, (b) 25.6 × 25.6, (c) 12.8 × 12.8, (d) 6.4 × 6.4, and (e) 1.6 × 1.6 km^2. The two different mass categories are defined according to a 40-μm threshold for drop radius. To better display the oscillations, we focus on 4 hr of the simulation (4–8 hr).

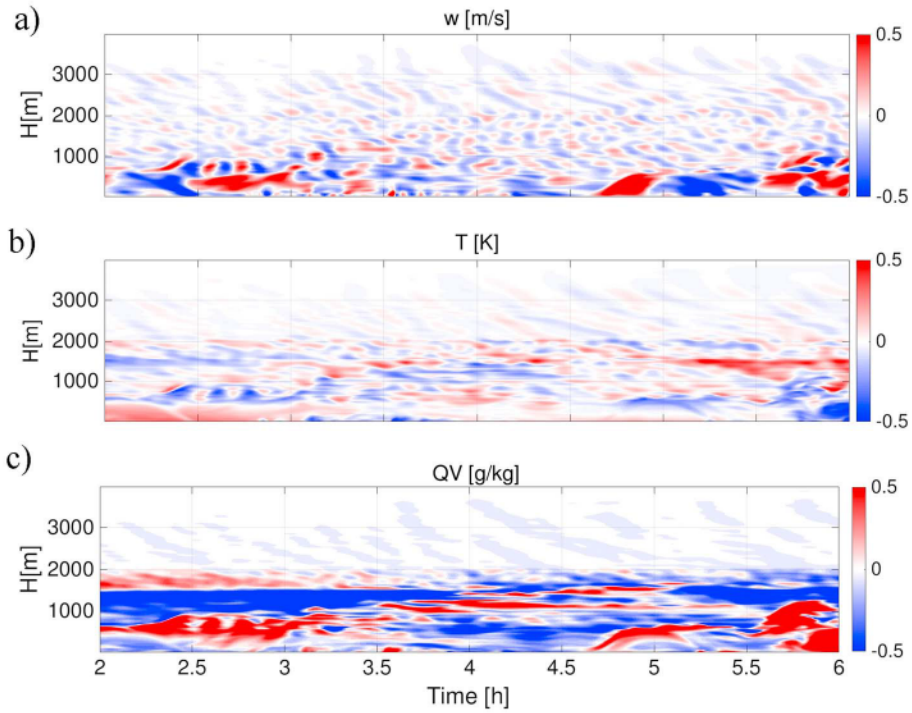

Figure 9. Evolution in a single column (in the middle of the large domain simulation with aerosol concentration of 500 cm^{-3}) of the vertical profile of (a) air vertical velocity (*w*), (b) temperature perturbation (*T*; i.e., deviation from the mean vertical profile), and (c) water vapor mixing ratio perturbation (QV). To better display the oscillations, we focus on 4 hr of the simulation (2–6 hr).

(Figure 8d) reveals apparent oscillations. However, decreasing the window size to a typical cloud size (1.6 × 1.6 km^2, Figure 8e) enables inspecting the local development of a single cloud at a time.

As for the higher-frequency cases in the nonprecipitating simulations, a hint of the controlling mechanism can be gleaned by following the vertical velocity in a single column located in the middle of the large domain simulation with aerosol concentration of 500 cm^{-3} and no winds (Figure 9a). It reveals oscillations with a typical period of ~10 min, which are noteworthy above the cloud base height (~500 m).

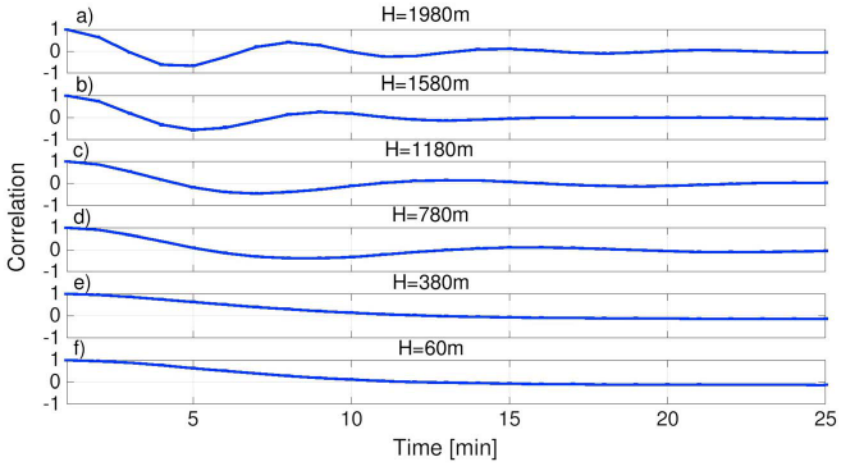

Figure 10. Mean over all grid points at a given vertical level (262,144 points) autocorrelation of the air vertical velocity over the last 80 min of the simulation (between 400 and 480 min) for different vertical levels (*H*): (a) 1,980, (b) 1,580, (c) 1,180, (d) 780, (e) 380, and (f) 60 m. Results are from the simulation with aerosol concentration of 500 cm^{-3}, large domain.

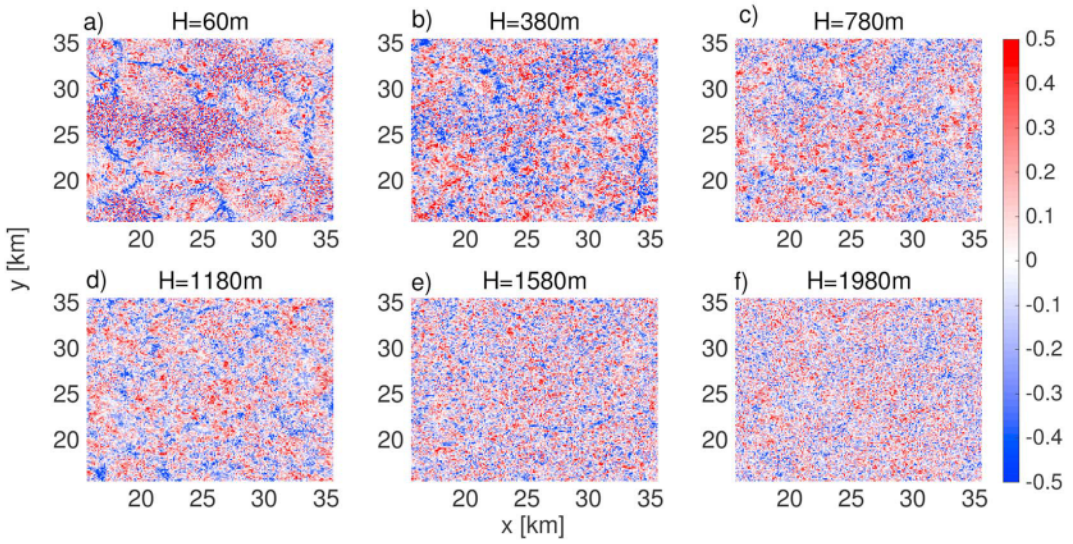

Figure 11. Spatial correlation of the air vertical velocity over the last 80 min of the simulation (between 400 and 480 min) for different vertical levels (*H*): (a) 60, (b) 380, (c) 780, (d) 1,180, (e) 1,580, (f) 1,980 m. Results are from the simulation with aerosol concentration of 5 cm^{-3}, large domain. To display the structures, we focus on the middle 20 × 20 km^2 of the domain. The correlations are calculated compared to the middle point of the domain.

Autocorrelation of the vertical velocity average over all grid points (512 × 512) for a few vertical levels (Figure 10) during the last 80 min of the simulation (between 400 and 480 min) shows significant time oscillations at the upper cloudy and inversion layers (Figures 10a and 10b). These oscillations are discernible all the way down to the lower cloudy layer (Figures 10c and 10d) but disappear below the cloud base (Figures 10e and 10f). These high-frequency oscillations are generated by gravity waves, as shown in previous works (Atkinson & Zhang, 1996; Clark et al., 1986; Huang, 1990), where they were seen to be initiated by cloud updrafts penetrating the stable inversion layer. The ~10-min frequency of these oscillations corresponds to the predicted frequency calculated according to the Brunt-Väisälä oscillations (the calculated gravity wave frequency—*N*, which is between 10 and 12 min depending on the height, Nappo, 2013):

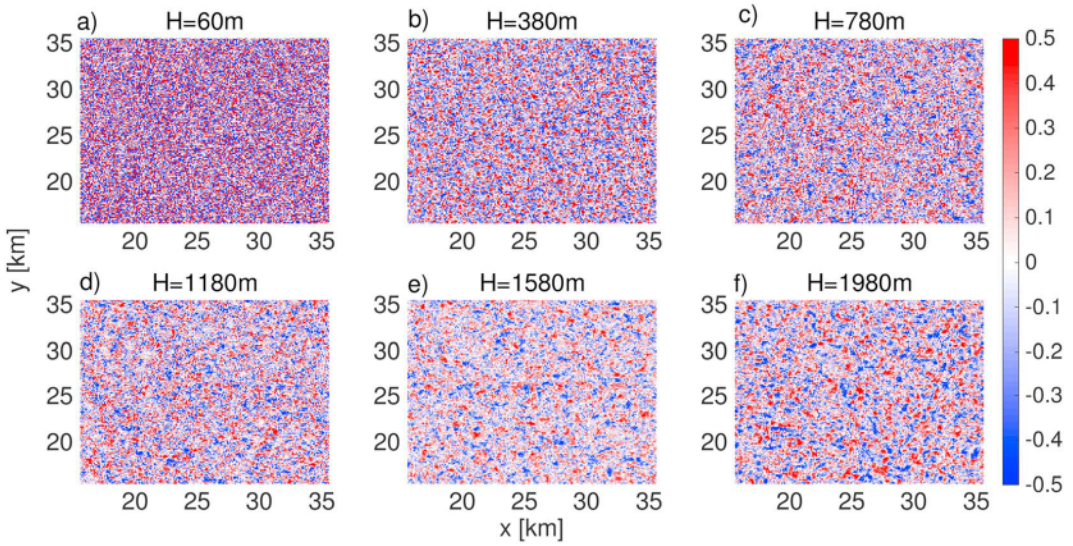

Figure 12. Same as Figure 11 but for the simulation with aerosol concentration of 500 cm^{-3}, large domain.

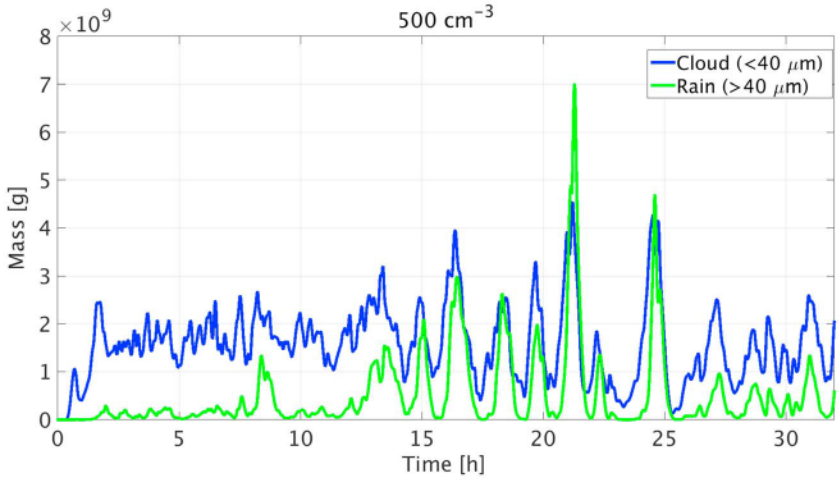

Figure 13. Evolution of the total cloud and rain masses in the domain for the simulation with aerosol concentration of 500 cm^{-3} and long simulation period of 32 hr. The two different mass categories are defined according to a 40-μm threshold for drop radius.

$$N = \left(\frac{g}{\theta_v}\frac{\partial \theta_v}{\partial z}\right)^{0.5} \quad (1)$$

where g is the gravitational acceleration, θ_v is the potential virtual temperature, and z is the vertical coordinate. The gravity waves perturb the vertical wind (Figure 9a), temperature (Figure 9b), and humidity (Figure 9c) fields and hence influence cloud development (Atkinson & Zhang, 1996; Clark et al., 1986; Huang, 1990).

To exclude effects of the domain's upper boundary, we implemented a damping layer at the top of the domain (Khairoutdinov & Randall, 2003). We also conducted an additional simulation with aerosol concentration of 500 cm^{-3} for a domain with double the vertical extent (8 km). It showed that even for the higher domain, the gravity waves are noticeable (Figure S2), suggesting no important contribution from the upper boundary of the simulated domain.

The spatial correlation of the vertical velocity for clean (Figure 11) and polluted (Figure 12) conditions (for a few vertical levels) reveals the different organization mechanisms in those two cases. Under polluted conditions, no significant spatial organization is apparent in the lower vertical levels (Figures 12a and 12b). Moving higher in the atmosphere reveals some spatial structures in the vertical velocity field, which are most noteworthy at the upper cloudy and inversion layers (Figures 12e and 12f). This shows that in the polluted nonprecipitating simulation, the organization is generated in the upper part (driven by gravity waves) and propagates somewhat downward. On the other hand, under clean conditions, a clear structure in the vertical velocity spatial correlation is observed near the surface. This large-scale structure is driven by cold pools (as was shown above). The organization for the clean cases is generated mainly in the low levels and only slightly modulated by the gravity waves from above (see slight organization in Figure 11f). The difference in the generation of gravity waves between the clean and polluted conditions can be attributed to the difference in updraft magnitude. Under polluted nonprecipitating conditions, the updrafts are stronger (compared to the clean case, Dagan et al., 2017) and the droplet mobility is larger (smaller droplets are pushed higher in the atmosphere, Dagan et al., 2018; Koren et al., 2015) and hence they penetrate the inversion layer more extensively and generate more significant gravity waves (see the difference between Figures 11f and 12f).

We showed that under polluted conditions, the high-frequency oscillations are dominant and the absence of precipitation results in deepening of the cloudy layer and destabilization of the atmosphere (Dagan et al., 2016). However, given enough time for the polluted clouds to cool and moisten the upper cloudy layer, thereby deepening it, precipitation can start (Seifert et al., 2015) and the low-frequency oscillations can become dominant. To examine this effect, we conducted an additional simulation of prolonged duration (32 hr for the simulation with aerosol loading of 500 cm^{-3}).

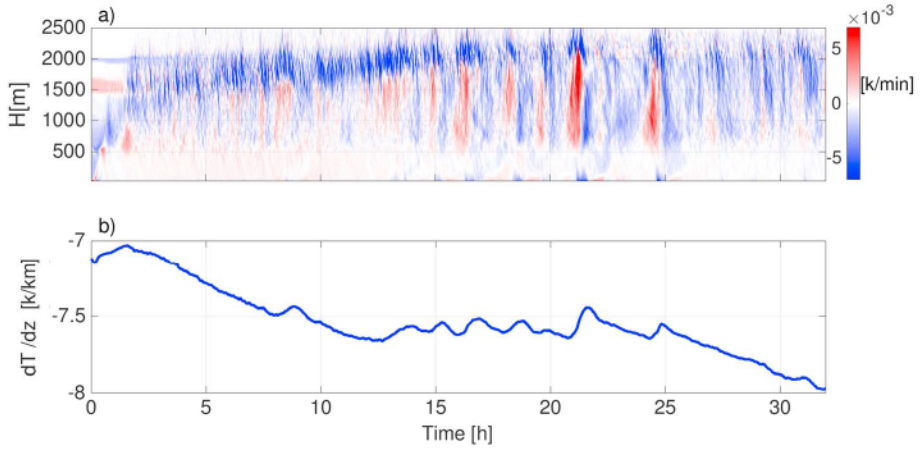

Figure 14. Temporal evolution of (a) the change in mean temperature vertical profile in the domain (K/min) for the simulation with aerosol concentration of 500 cm^{-3} and long simulation period of 32 hr; (b) the temperature lapse rate between the initial inversion base height (H = 1,500 m) and the lowest atmospheric grid cell (H = 20 m).

Prolonging the simulation (Figure 13) revealed substantial low-frequency oscillations, which started after ~13 hr of simulation (see also Figure S4 in the supporting information). Monitoring the thermodynamic conditions along the simulation (Figures 14 and S3 in the supporting information) demonstrated that indeed the cloudy layer deepens and the instability increases (Dagan et al., 2016). Once the rain becomes significant, the destabilization process declines.

4. Summary

The evolution of water mass in simulated shallow, warm convective cloud fields was followed and revealed temporal oscillations. For the case studied here, these oscillations were shown to have two distinct periods of ~90 and ~10 min. Under precipitating conditions, the low-frequency oscillations dominate and express cycles of *recharge-discharge* of the thermodynamic instability. Net condensation at the cloudy layer and net evaporation below the cloud base during rain phases act to stabilize the lower atmosphere. This further restricts cloud and rain development, which then enables the surface fluxes to rebuild the instability.

Under nonprecipitating conditions, the high frequency dominates. The source of the high-frequency oscillations are gravity waves that are produced by updrafts penetrating the stable inversion layer (Atkinson & Zhang, 1996; Clark et al., 1986; Huang, 1990). These gravity waves modulate both the dynamic (i.e., vertical velocity) and thermodynamic (i.e., temperature and humidity) fields and hence control cloud development. This mechanism controls the self-organization of the cloud field as long as rain is absent. Once the thermodynamic instability increases and the cloudy layer deepens sufficiently (Dagan et al., 2016) to produce significant precipitation, the cloud field will be pushed toward the low-frequency oscillations. In a large enough domain (~50 km), these oscillations average out. The preferred spatial scale for observing these oscillations is ~10 km, which is larger than that of a single, warm convective cloud but local enough to capture the dominant oscillation phase.

The values of both the high- and low-frequency oscillation periods (10 and 90 min, respectively, for this study) depend on the thermodynamic conditions such as instability, inversion base height, and large-scale forcing. However, we suggest that the general behavior of these two different regimes of precipitating and nonprecipitating conditions (low- and high-frequency oscillations, respectively) is universal. Moreover, limitations of LES models, such as those caused by the impact of the double periodic boundary conditions on the cold pools' dynamics, can also affect the estimated period of oscillations.

Physical insights into the mechanisms controlling self-organization of warm convective cloud fields can improve our understanding of cloud-aerosol interactions in these cloud types (Seifert et al., 2015) and low-cloud feedback under climate change (Vogel et al., 2016).

Acknowledgments
This research was supported by the Ministry of Science and Technology, Israel (grant 3-14444). Key parameters from the simulated data are available at https://weizmann.alma.exlibrisgroup.com/view/delivery/972WIS_INST/992868619803596.

References

Altaratz, O., Koren, I., Reisin, T., Kostinski, A., Feingold, G., Levin, Z., & Yin, Y. (2008). Aerosols' influence on the interplay between condensation, evaporation and rain in warm cumulus cloud. *Atmospheric Chemistry and Physics*, *8*(1), 15–24. https://doi.org/10.5194/acp-8-15-2008

Atkinson, B., & Zhang, J. W. (1996). Mesoscale shallow convection in the atmosphere. *Reviews of Geophysics*, *34*(4), 403–431. https://doi.org/10.1029/96RG02623

Benedict, J. J., & Randall, D. A. (2007). Observed characteristics of the MJO relative to maximum rainfall. *Journal of the Atmospheric Sciences*, *64*(7), 2332–2354. https://doi.org/10.1175/JAS3968.1

Bladé, I., & Hartmann, D. L. (1993). Tropical intraseasonal oscillations in a simple nonlinear model. *Journal of the Atmospheric Sciences*, *50*(17), 2922–2939. https://doi.org/10.1175/1520-0469(1993)050<2922:TIOIAS>2.0.CO;2

Bony, S., & Dufresne, J. L. (2005). Marine boundary layer clouds at the heart of tropical cloud feedback uncertainties in climate models. *Geophysical Research Letters*, *32*, L20806. https://doi.org/10.1029/2005GL023851

Clark, T. L., Hauf, T., & Kuettner, J. P. (1986). Convectively forced internal gravity waves: Results from two-dimensional numerical experiments. *Quarterly Journal of the Royal Meteorological Society*, *112*(474), 899–925. https://doi.org/10.1002/qj.49711247402

Dagan, G., Koren, I., & Altaratz, O. (2015a). Aerosol effects on the timing of warm rain processes. *Geophysical Research Letters*, *42*, 4590–4598. https://doi.org/10.1002/2015GL063839

Dagan, G., Koren, I., & Altaratz, O. (2015b). Competition between core and periphery-based processes in warm convective clouds–from invigoration to suppression. *Atmospheric Chemistry and Physics*, *15*(5), 2749–2760. https://doi.org/10.5194/acp-15-2749-2015

Dagan, G., Koren, I., & Altaratz, O. (2018). Quantifying the effect of aerosol on vertical velocity and effective terminal velocity in warm convective clouds. *Atmospheric Chemistry and Physics*, *18*(9), 6761–6769. https://doi.org/10.5194/acp-18-6761-2018

Dagan, G., Koren, I., Altaratz, O., & Heiblum, R. H. (2016). Aerosol effect on the evolution of the thermodynamic properties of warm convective cloud fields. *Scientific Reports*, *6*(1), 38769. https://doi.org/10.1038/srep38769

Dagan, G., Koren, I., Altaratz, O., & Heiblum, R. H. (2017). Time-dependent, non-monotonic response of warm convective cloud fields to changes in aerosol loading. *Atmospheric Chemistry and Physics*, *17*(12), 7435–7444. https://doi.org/10.5194/acp-17-7435-2017

Dey, S., Di Girolamo, L., Zhao, G., Jones, A. L., & McFarquhar, G. M. (2011). Satellite-observed relationships between aerosol and trade-wind cumulus cloud properties over the Indian Ocean. *Geophysical Research Letters*, *38*, L01804. https://doi.org/10.1029/2010GL045588

Feingold, G., & Koren, I. (2013). A model of coupled oscillators applied to the aerosol–cloud–precipitation system. *Nonlinear Processes in Geophysics*, *20*(6), 1011–1021. https://doi.org/10.5194/npg-20-1011-2013

Feingold, G., Koren, I., Wang, H., Xue, H., & Brewer, W. A. (2010). Precipitation-generated oscillations in open cellular cloud fields. *Nature*, *466*(7308), 849–852. https://doi.org/10.1038/nature09314

Goren, T., & Rosenfeld, D. (2012). Satellite observations of ship emission induced transitions from broken to closed cell marine stratocumulus over large areas. *Journal of Geophysical Research*, *117*, D17206. https://doi.org/10.1029/2012JD017981

Heiblum, R. H., Altaratz, O., Koren, I., Feingold, G., Kostinski, A. B., Khain, A. P., et al. (2016). Characterization of cumulus cloud fields using trajectories in the center of gravity versus water mass phase space: 2. Aerosol effects on warm convective clouds. *Journal of Geophysical Research: Atmospheres*, *121*, 6356–6373. https://doi.org/10.1002/2015JD024193

Holland, J. Z., & Rasmusson, E. M. (1973). Measurements of the atmospheric mass, energy, and momentum budgets over a 500-kilometer square of tropical ocean. *Monthly Weather Review*, *101*(1), 44–55. https://doi.org/10.1175/1520-0493(1973)101<0044:MOTAME>2.3.CO;2

Huang, X.-Y. (1990). The organization of moist convection by internal gravity waves. *Tellus A: Dynamic Meteorology and Oceanography*, *42*(2), 270–285. https://doi.org/10.3402/tellusa.v42i2.11877

Jaenicke, R. (1988). Aerosol physics and chemistry. In G. Fischer (Ed.), *Meterology Landolt-Börnstein, New Ser*. (Vol. 4b, edited by, pp. 391–457). Berlin: Springer.

Jiang, H., Xue, H., Teller, A., Feingold, G., & Levin, Z. (2006). Aerosol effects on the lifetime of shallow cumulus. *Geophysical Research Letters*, *33*, L14806. https://doi.org/10.1029/2006GL026024

Khain, A., Ovtchinnikov, M., Pinsky, M., Pokrovsky, A., & Krugliak, H. (2000). Notes on the state-of-the-art numerical modeling of cloud microphysics. *Atmospheric Research*, *55*(3–4), 159–224. https://doi.org/10.1016/S0169-8095(00)00064-8

Khain, A., & Pokrovsky, A. (2004). Simulation of effects of atmospheric aerosols on deep turbulent convective clouds using a spectral microphysics mixed-phase cumulus cloud model. Part II: Sensitivity study. *Journal of the Atmospheric Sciences*, *61*(24), 2983–3001. https://doi.org/10.1175/JAS-3281.1

Khairoutdinov, M. F., & Randall, D. A. (2003). Cloud resolving modeling of the ARM summer 1997 IOP: Model formulation, results, uncertainties, and sensitivities. *Journal of the Atmospheric Sciences*, *60*(4), 607–625. https://doi.org/10.1175/1520-0469(2003)060<0607:CRMOTA>2.0.CO;2

Koren, I., Altaratz, O., & Dagan, G. (2015). Aerosol effect on the mobility of cloud droplets. *Environmental Research Letters*, *10*(10), 104011. https://doi.org/10.1088/1748-9326/10/10/104011

Koren, I., Dagan, G., & Altaratz, O. (2014). From aerosol-limited to invigoration of warm convective clouds. *Science*, *344*(6188), 1143–1146. https://doi.org/10.1126/science.1252595

Koren, I., & Feingold, G. (2011). Aerosol-cloud-precipitation system as a predator-prey problem. *Proceedings of the National Academy of Sciences of the United States of America*, *108*(30), 12,227–12,232. https://doi.org/10.1073/pnas.1101777108

Koren, I., & Feingold, G. (2013). Adaptive behavior of marine cellular clouds. *Scientific Reports*, *3*(1). https://doi.org/10.1038/srep02507

Koren, I., Tziperman, E., & Feingold, G. (2017). Exploring the nonlinear cloud and rain equation. *Chaos: An Interdisciplinary Journal of Nonlinear Science*, *27*(1), 013107. https://doi.org/10.1063/1.4973593

Malkus, J. S., & Riehl, H. (1964). Cloud structure and distributions over the tropical Pacific Ocean. *Tellus*, *16*(3), 275–287. https://doi.org/10.1111/j.2153-3490.1964.tb00167.x

Nair, U., Weger, R., Kuo, K., & Welch, R. (1998). Clustering, randomness, and regularity in cloud fields: 5. The nature of regular cumulus cloud fields. *Journal of Geophysical Research*, *103*(D10), 11,363–11,380. https://doi.org/10.1029/98JD00088

Nappo, C. J. (2013). *An introduction to atmospheric gravity waves*. London, UK: Academic Press.

Norris, J. R. (1998). Low cloud type over the ocean from surface observations. Part II: Geographical and seasonal variations. *Journal of Climate*, *11*(3), 383–403. https://doi.org/10.1175/1520-0442(1998)011<0383:LCTOTO>2.0.CO;2

Platnick, S., King, M. D., Ackerman, S. A., Menzel, W. P., Baum, B. A., Riedi, J. C., & Frey, R. A. (2003). The MODIS cloud products: Algorithms and examples from Terra. *IEEE Transactions on Geoscience and Remote Sensing*, *41*(2), 459–473. https://doi.org/10.1109/TGRS.2002.808301

Rosenfeld, D. (1999). TRMM observed first direct evidence of smoke from forest fires inhibiting rainfall. *Geophysical Research Letters*, *26*(20), 3105–3108. https://doi.org/10.1029/1999GL006066

Rosenfeld, D., Kaufman, Y. J., & Koren, I. (2006). Switching cloud cover and dynamical regimes from open to closed Benard cells in response to the suppression of precipitation by aerosols. *Atmospheric Chemistry and Physics*, *6*(9), 2503–2511. https://doi.org/10.5194/acp-6-2503-2006

Rosenfeld, D., Wood, R., Donner, L. J., & Sherwood, S. C. (2013). Aerosol cloud-mediated radiative forcing: Highly uncertain and opposite effects from shallow and deep clouds. In *Climate science for serving society*, edited (pp. 105–149). London: Springer.

Sato, Y., Shima, S., & Tomita, H. (2018). Numerical convergence of shallow convection cloud field simulations: Comparison between double-moment Eulerian and particle-based Lagrangian microphysics coupled to the same dynamical core. *Journal of Advances in Modeling Earth Systems*, *10*, 1495–1512. https://doi.org/10.1029/2018MS001285

Sato, Y., Shima, S. i., & Tomita, H. (2017). A grid refinement study of trade wind cumuli simulated by a Lagrangian cloud microphysical model: The super-droplet method. *Atmospheric Science Letters*, *18*(9), 359–365. https://doi.org/10.1002/asl.764

Savane, O. S., Vant-Hull, B., Mahani, S., & Khanbilvardi, R. (2015). Effects of aerosol on cloud liquid water path: Statistical method a potential source for divergence in past observation based correlative studies. *Atmosphere*, *6*(3), 273–298. https://doi.org/10.3390/atmos6030273

Seifert, A., & Heus, T. (2013). Large-eddy simulation of organized precipitating trade wind cumulus clouds. *Atmospheric Chemistry and Physics*, *13*(11), 5631–5645. https://doi.org/10.5194/acp-13-5631-2013

Seifert, A., Heus, T., Pincus, R., & Stevens, B. (2015). Large-eddy simulation of the transient and near-equilibrium behavior of precipitating shallow convection. *Journal of Advances in Modeling Earth Systems*, *7*, 1918–1937. https://doi.org/10.1002/2015MS000489

Seigel, R. B. (2014). Shallow cumulus mixing and subcloud layer responses to variations in aerosol loading. *Journal of the Atmospheric Sciences (2014)*, *71*(7), 2581–2603. https://doi.org/10.1175/JAS-D-13-0352.1

Siebesma, A. P., Bretherton, C. S., Brown, A., Chlond, A., Cuxart, J., Duynkerke, P. G., et al. (2003). A large eddy simulation intercomparison study of shallow cumulus convection. *Journal of the Atmospheric Sciences*, *60*(10), 1201–1219. https://doi.org/10.1175/1520-0469(2003)60<1201:ALESIS>2.0.CO;2

Small, J. D., Chuang, P. Y., Feingold, G., & Jiang, H. (2009). Can aerosol decrease cloud lifetime? *Geophysical Research Letters*, *36*, L16806. https://doi.org/10.1029/2009GL038888

Thayer-Calder, K., & Randall, D. A. (2009). The role of convective moistening in the Madden–Julian oscillation. *Journal of the Atmospheric Sciences*, *66*(11), 3297–3312. https://doi.org/10.1175/2009JAS3081.1

Vogel, R., Nuijens, L., & Stevens, B. (2016). The role of precipitation and spatial organization in the response of trade-wind clouds to warming. *Journal of Advances in Modeling Earth Systems*, *8*, 843–862. https://doi.org/10.1002/2015MS000568

Webb, M., Senior, C., Sexton, D., Ingram, W., Williams, K., Ringer, M., et al. (2006). On the contribution of local feedback mechanisms to the range of climate sensitivity in two GCM ensembles. *Climate Dynamics*, *27*(1), 17–38. https://doi.org/10.1007/s00382-006-0111-2

Xue, H. W., & Feingold, G. (2006). Large-eddy simulations of trade wind cumuli: Investigation of aerosol indirect effects. *Journal of the Atmospheric Sciences*, *63*(6), 1605–1622. https://doi.org/10.1175/JAS3706.1

Xue, H. W., Feingold, G., & Stevens, B. (2008). Aerosol effects on clouds, precipitation, and the organization of shallow cumulus convection. *Journal of the Atmospheric Sciences*, *65*(2), 392–406. https://doi.org/10.1175/2007JAS2428.1

Yano, J. I., & Plant, R. (2012). Finite departure from convective quasi-equilibrium: Periodic cycle and discharge–recharge mechanism. *Quarterly Journal of the Royal Meteorological Society*, *138*(664), 626–637. https://doi.org/10.1002/qj.957

Yuan, T., Remer, L. A., & Yu, H. (2011). Microphysical, macrophysical and radiative signatures of volcanic aerosols in trade wind cumulus observed by the A-train. *Atmospheric Chemistry and Physics*, *11*(14), 7119–7132. https://doi.org/10.5194/acp-11-7119-2011

Zuidema, P., Li, Z., Hill, R. J., Bariteau, L., Rilling, B., Fairall, C., et al. (2012). On trade wind cumulus cold pools. *Journal of the Atmospheric Sciences*, *69*(1), 258–280. https://doi.org/10.1175/JAS-D-11-0143.1